A piezoelectric catalytic cascade nanoreactor which reshapes the tumor microenvironment and promotes effective multi-dimensional therapy

Yilu Zheng[1], Yichao Du[5], Gareth R. Williams[3], Ying Zhu[4], Tong Wang[1], Yanyan Zhang[1], Jianxiang Xu[1], Junzi Wu*[4], Fan Li*[2], Li-Min Zhu*[1]

[1] College of Biological Science and Medical Engineering, Shanghai Engineering Research Center of Nano-Biomaterials and Regenerative Medicine, Donghua University, Shanghai 201620, P.R. China

[2] Department of Ultrasound, Shanghai General Hospital, Shanghai Jiao Tong University School of Medicine，Shanghai，201620，PR. China

[3] UCL School of Pharmacy, University College London, 29-39 Brunswick Square, London WC1N 1AX, UK

[4] The Key Laboratory of Microcosmic Syndrome Differentiation, Education Department of Yunnan, Yunnan University of Traditional Chinese Medicine, Kunming 650500, P.R. China

[5] Department of Surgery, Shanghai General Hospital, Shanghai Jiao Tong University School of Medicine，Shanghai，201620，PR. China

*Corresponding authors: xnfz@ynutcm.edu.cn (J. Wu), medicineli@163.com (F. Li), lzhu@dhu.edu.cn (L.-M. Zhu).

Abstract: The nature of the tumor microenvironment (TME) is often a hindrance to effective cancer therapy and results in treatment failure. Here, a nanoparticle cascade catalyst has been developed. This platform, Ber/$CoFe_2O_4$@$PSiO_2$-KCN, is based on $CoFe_2O_4$ nanoparticles which are then coated with silica, functionalized with potassium doped carbon nitride (KCN) and loaded with the drug berberine (Ber). Ber/$CoFe_2O_4$@$PSiO_2$-KCN in combination with ultrasound is found to have the ability to generate gluconic acid and H_2O_2 from glucose and convert H_2O_2 to ·OH to provide effective chemodynamic therapy. Ber promotes the accumulation of lactic acid in tumor cells, acidifying the TME and facilitating the catalytic reactions of KCN and $CoFe_2O_4$. The oxidative stress generated by the presence of large amounts of ·OH in the tumor triggers cell apoptosis, the production of damage-associated molecular pathways, and thus induces immunogenic cell death. The potent anti-tumor effects and imaging function of Ber/$CoFe_2O_4$@$PSiO_2$-KCN could be applied as a future anti-cancer therapy.

Keywords: Acid accumulation; Catalyze; Chemodynamic therapy; Cancer immunotherapy

1 Introduction

The presence of nutrients such as glucose and various amino acids in the tumor environment enables rapid growth[1-3]. Recently, the regulation of nutrient metabolism in cancer cells has been shown to hold great promise for achieving effective tumor suppression[3, 4]. The energy requirements of tumors are significant, and under aerobic glycolysis glucose acts as a pillar of tumor metabolism to produce adenosine triphosphate (ATP) and lactate[5]. Lactate is then exported from cancer cells via the monocarboxylate transporter protein (MCT). Increasing amounts of evidence show that lactate can promote the phagocytosis of tumor cells by dendritic cells (DC) and stimulate DC maturation[6, 7]. Therefore, lactate accumulation can help to reduce the immunosuppressive nature of the tumor microenvironment (TME) and thus increase the efficacy of cancer therapies.

In recent years, cancer starvation therapy based on glucose deprivation has generated interest in the community[8-10]. Glucose oxidase (GOx) or glucose oxidation mimetic enzyme can catalyze the reaction of glucose to produce gluconic acid and hydrogen peroxide (H_2O_2).[11-13] The use of glucose oxidation enzymes to catalyze the production of H_2O_2 can serve as a source of ROS, continuously providing substrate H_2O_2.[14] H_2O_2 can be further applied to accelerate other anti-cancer treatments, such as chemodynamic therapy (CDT) and chemotherapy, which act synergistically with glucose depletion. CDT has been increasingly explored in recent years, and relies on the generation of reactive oxygen species (ROS) via the chemical reaction of H_2O_2[15-17]. The therapeutic effect of endogenous CDT is significantly curtailed by the limited availability of active oxygen sources in the tumor, which will in turn limit the production of cytotoxic ROS [18, 19]. This

challenge can be overcome through the intelligent design of nanomedicines, however. With advancements in functional nanomaterials, we have witnessed the successful fabrication of various iron-based nanomaterials which can catalyze the Fenton reaction and thereby enhance CDT therapy and other cancer treatments [20].

Several pioneering studies have revealed that cellular debris remaining after CDT ablation of tumors can trigger immunogenic cell death (ICD)[21, 22]. Nutrient attenuation or tumor acidity regulation may also improve the potency of CDT by reversing tumor immunosuppression to more effectively treat metastatic tumors [21]. However, while current iron-based materials for CDT therapy show promise, there is an urgent need to develop a system that alters the endogenous environment to trigger catalysis. The development of advanced materials to catalyze reactions in cascades is a common means, and can be achieved by the combination of iron-based materials with other metals to exert enhanced CDT effects[23, 24]. To date, there are relatively few studies exploring the use of iron-based materials combined with carbon materials to catalyze the conversion of glucose to gluconic acid and hydrogen peroxide.

Here, we designed a ROS cascade nanoplatform, Ber/$CoFe_2O_4$@$PSiO_2$-KCN, that shows powerful synergistic antitumor effects by combining a potassium doped carbon nitride (KCN) based glucose catalytic system with a $CoFe_2O_4$-based CDT agent and loading the drug berberine (Ber). In the design, the piezoelectric properties of KCN are exploited to continuously convert glucose into H_2O_2 and gluconic acid. KCN's ability to convert the mechanical energy of ultrasound into chemical energy means that the application of the former can enhance the efficacy of CDT. The H_2O_2 in the tumor and the aforementioned supplementary H_2O_2 are converted into cytotoxic hydroxyl radicals (•OH) by $CoFe_2O_4$ through the Fenton reaction. The presence of these reactive oxygen species (ROS) consumes glutathione (GSH) in tumor cells, causing cell death via the ferroptosis pathway (which results from Fe-dependent lipid peroxidation). At the same time, Ber inhibits mitochondrial complex I, which leads to intracellular lactic acid accumulation. This, combined with the gluconic acid generated by KCN, together increase the acidity in the tumor cells, which accelerates the Fenton reaction. This ROS production further excites ICD in tumors, leading to greater immune cell infiltration, and activating an anti-tumor immune response. In addition, the nanosystem has magnetic resonance (MR) imaging properties, permitting the integration of tumor diagnosis and treatment.

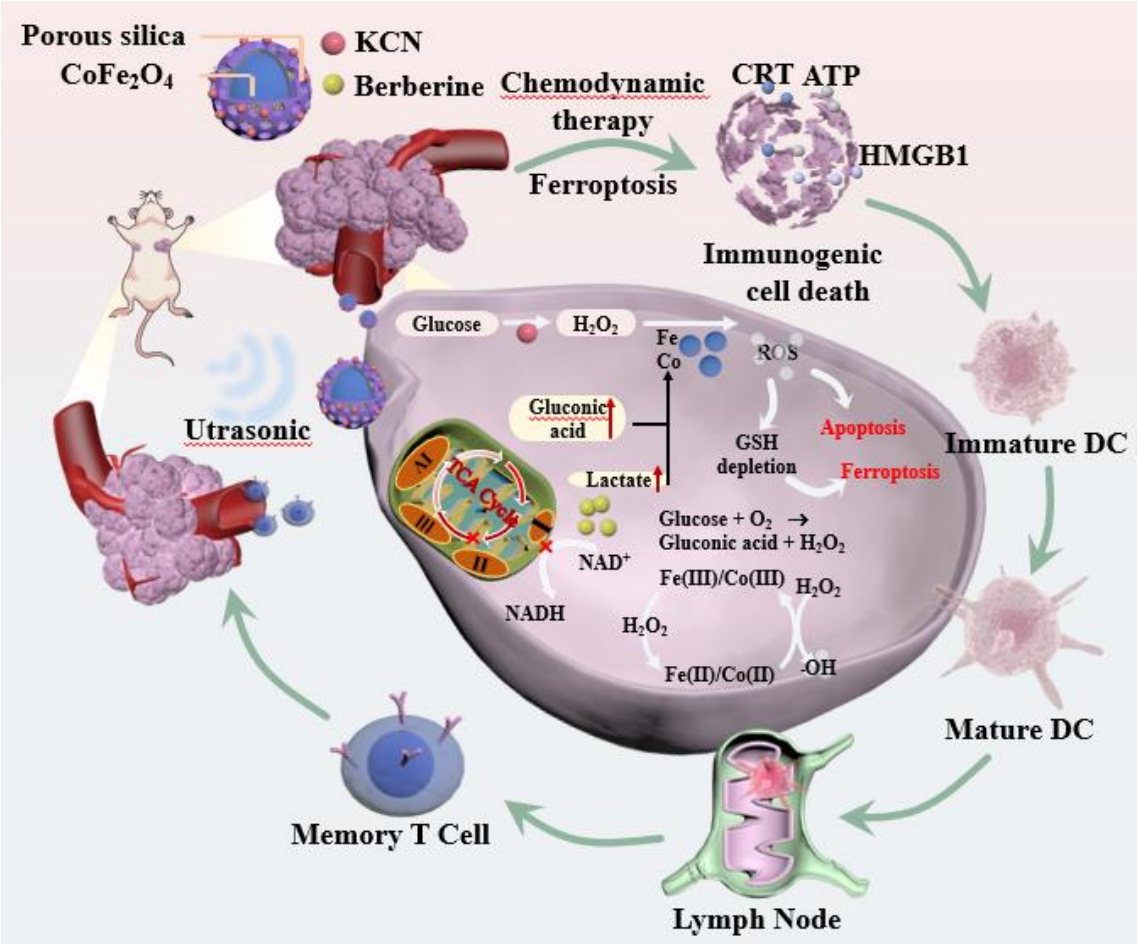

Scheme 1. The mechanism by which the Ber/$CoFe_2O_4$@$PSiO_2$-KCN system enhances tumor therapy via a catalytic cascade.

2 Results and discussion

2.1 Characterization

$CoFe_2O_4$ nanoparticles were synthesized using a hydrothermal method, which was followed by a series of modifications (Fig. 1A). Silica and porous silica shells were first deposited by a two-step sol-gel method to obtain $CoFe_2O_4$@PSi nanoparticles (Fig. 1A). After carboxylation on the surface of the $CoFe_2O_4$@PSi nanoparticles to form $CoFe_2O_4$@PSiC, KCN was attached through EDC coupling. Transmission electron microscopy (TEM) images of KCN and $CoFe_2O_4$@PSiC-KCN are presented in Fig. 1(B) and (C) respectively. The suspension of KCN exhibited a significant Tyndall effect (Fig. 1B), and there is clear core-shell structure evident for $CoFe_2O_4$@PSiC-KCN. The particle sizes of KCN and $CoFe_2O_4$@PSiC-KCN were estimated to be ~3 nm and 100-200 nm, respectively. An element mapping image indicates uniform distribution of N, O, Co, Fe, Si, and K elements in $CoFe_2O_4$@PSiC-KCN NPs. Moreover, the distribution radius of Si and O is

larger than that of Co and Fe, indicating that the PSiC coating has successfully encapsulated $CoFe_2O_4$ (Fig. S1). K is uniformly distributed on the exterior of the nanoparticles, indicating that KCN is successfully connected to the $CoFe_2O_4$@PSiC. The particle size of $CoFe_2O_4$@PSiC-KCN (≈ 146 nm) was determined from dynamic light scattering measurements (Fig. S2). This is higher than that observed by TEM, due to the presence of a water layer around the nanoparticles in DLS. The zeta potential of the $CoFe_2O_4$NPs was -18.7 ± 0.9 mV (Fig. 1D). This is likely to be because the stabilizer sodium acetate adsorbs to the surface of the NPs, resulting in the presence of COO^- groups at the particle exterior. The potential increases to +3.1 ± 0.9 mV after adding the silica shell as the COO^- surface groups are replaced by less acidic groups.[25] Due to the presence of a large number of amino groups on the surface of KCN particles, after modification with KCN, the potential changed to +1.1 ± 0.3 mV. Figure S3 (Supplementary Information) shows the X-ray diffraction (XRD) patterns of $CoFe_2O_4$ and KCN. XRD data for $CoFe_2O_4$@PSiC-KCN (Fig. 1E) reveal the presence of $CoFe_2O_4$ Bragg reflections at 2θ=18.07°, 30.52°, 35.71°, 43.75°, 53.36°, 56.97°, 62.48°. A reflection at 29.82° is the (002) reflection of KCN. These data are all consistent with the successful formation of the desired composite NPs.

The elemental content of $CoFe_2O_4$@PSiC-KN was analyzed by inductively coupled plasma-optical emission spectrometry (ICP-OES), and the results are summarized in the Supplementary Information, Table S1. The $CoFe_2O_4$@PSiC-KCN material contains Si, K, Fe and Co, confirming successful functionalization. X-ray photoelectron spectroscopy (XPS) results were used to analyze the surface composition of $CoFe_2O_4$@PSiC-KCN (Fig. 1F) and to determine the specific valence states (Fig. S4). Fig. 1F shows the coexistence of Fe, Co, C, N, K, O and Si in the NPs. The Fe 2p spectrum (Fig. S4A) can be deconvoluted into four peaks with peak shifts of 716.97, 713.87, 706.93 and 703.13 eV. These correspond to Fe^{3+} $2p_{1/2}$, Fe^{2+} $2p_{1/2}$, Fe^{3+} $2p_{3/2}$ and Fe^{2+} $2p_{3/2}$, respectively[26]. The XPS spectrum of Co 2p (Fig. S4B) can also be divided into four peaks arising from the presence of both Co^{2+} and Co^{3+} $2p_{3/2}$ and $2p_{1/2}$ bands. The binding energies at 772.85 and 788.96 eV were attributed to Co^{2+} $2p_{3/2}$ and $2p_{1/2}$, respectively, and two peaks at 793.18 and 775.40 eV were identified as the Co^{3+} bands (Fig. S4B)[27]. Peaks at 285.76 eV and 287.6 eV were assigned to the terminal C-NH_x of the heptazine unit in KCN Sand the sp^2 hybridized C atom (N-**C**=N)[28] (see also Fig. 1B, inset).

In the FTIR spectrum of $CoFe_2O_4$ (Fig. 1G), peaks at 1552 cm^{-1} and 1376 cm^{-1} arise from carboxylate groups on the surface after hydrothermal synthesis. There is a -OH vibration peak at 3330 cm^{-1}, and a band at 538 cm^{-1} arises from Fe-O vibrations [29]. Deposition of the SiO_2 layer results in a broad peak at 3300-3600 cm^{-1} from -OH vibrations of the silanol group (Si-OH), while a band at 954 cm^{-1} arises from the bending vibration of Si-OH. The absorption band at 1071 cm^{-1} is the Si-O-Si anti-symmetric stretching vibration. After KCN addition, a vibration at 1643 cm^{-1} from the amide group used to achieve coupling through EDC chemistry can be seen. There is a typical vibration of cyanide (-C≡N) at 2158 cm^{-1}. The peak at 806 cm^{-1} is distinctive of the tri-S-triazine group (C_6N_7) in KCN[30], while bands between 1200 - 1700 cm^{-1} are caused by

the stretching vibration of aromatic C-N heterocycles[31, 32].

The N_2 adsorption-desorption isotherm was determined and the $CoFe_2O_4$@PSiC-KCN specific surface area and pore diameter found to be 26.011 m^2/g and 3.826 nm, respectively (Fig. 1H). The curve shows a typical type IV plot, indicating that $CoFe_2O_4$@PSiC-KCN has a mesoporous structure. This was exploited for the absorption of Ber[33]. Successful loading of the drug can be seen from the UV spectra. $CoFe_2O_4$@PSiC-KCN shows no appreciable absorbance from 300 – 450 nm, while Ber has two peaks at ca. 345 and 421 nm (Fig. S5). Ber/ $CoFe_2O_4$@PSiC-KCN shows a distinctive Ber absorption peak at 344 nm (Fig. S5), confirming drug loading. The encapsulation efficiency and drug loading capacity of Ber were calculated to be 2.8 ± 0.8 % and 0.2 ± 0.0 %, respectively.

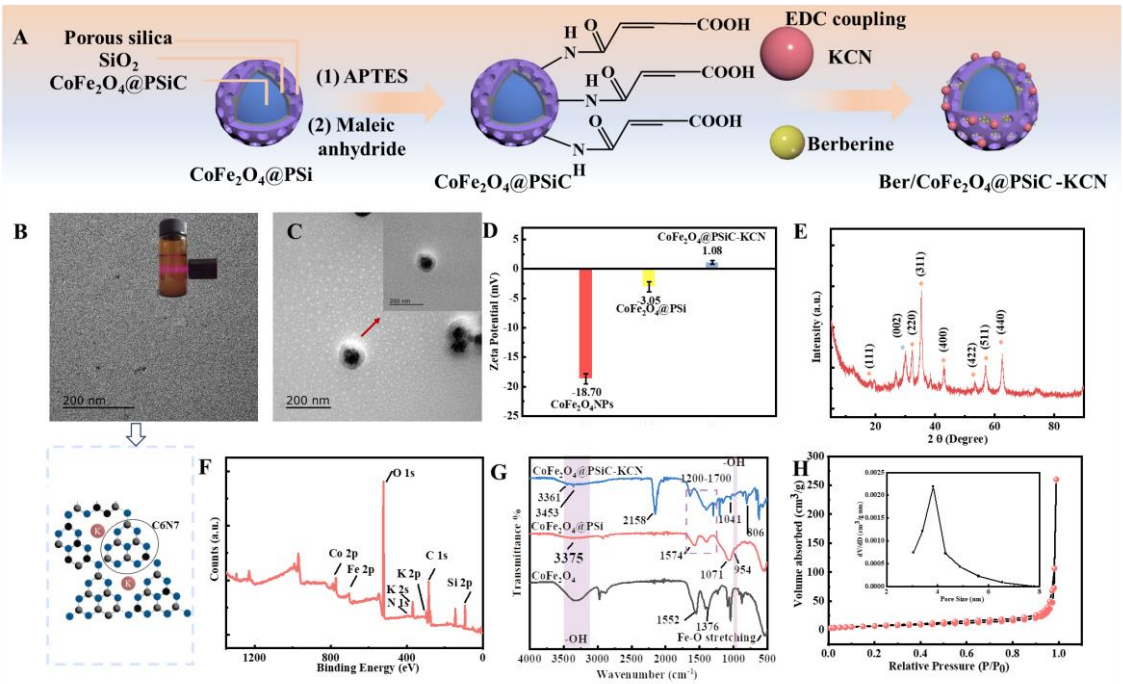

Figure 1 Characterization of $CoFe_2O_4$@PSiC-KCN. (A) The $CoFe_2O_4$@PSiC-KCN synthesis process. (B) TEM image of KCN (inset: schematic of the KCN structure. The vial inset shows a suspension of KCN quantum dots, and with a clear Tyndall effect visible). (C) TEM image of $CoFe_2O_4$@PSiC-KCN. (D) Zeta potential of the nanoparticles. (E) XRD pattern of $CoFe_2O_4$@PSiC-KCN. (F) Wide-field XPS spectrum of $CoFe_2O_4$@PSiC-KCN. (G) FTIR spectra of $CoFe_2O_4$, $CoFe_2O_4$@PSi and $CoFe_2O_4$@PSiC-KCN. (H) Nitrogen adsorption isotherm and pore size distribution of $CoFe_2O_4$@PSiC-KCN.

2.2 Enzyme-mimetic catalysis

When glucose oxidase is present, glucose in solution will be oxidized to H_2O_2 and gluconic acid (Fig. S6A). In this work, $CoFe_2O_4$@PSiC-KCN was used as a glucose oxidase mimetic enzyme to recapitulate the

catalytic function of the enzyme. $CoFe_2O_4$@PSiC-KCN was reacted with glucose solution at room temperature and exposure to ultrasound, and the rate of piezoelectric catalysis increased with the concentration of glucose in the range of 34.375 - 275 mM (Fig. 2A). The gluconic acid product of this reaction can easily be quantified by a colorimetric assay using hydroxylamine and $FeCl_3$ (Fig. S6B). When hydroxylamine and Fe^{3+} are added to the solution after reaction, the solution will change from colorless to orange if gluconic acid is present, and there will be a distinct absorption peak at 450-700 nm. The results (Fig. 2B) clearly demonstrate that successful catalysis was induced by the nanoplatform. If the solution obtained after piezoelectric catalysis is neutralized by NaOH, sodium gluconate can be identified by liquid chromatography-mass spectrometry (LC-MS). A distinct peak is observed at 0.208 min and a molecular weight of 218 Da (Fig. 2C, Fig. S7A, B). This confirms that gluconic acid has been generated.

The second product resulting from the catalytic reaction of glucose is H_2O_2. This can also be detected with a colorimetric assay, this time using tetramethylbenzidine (TMB) and horseradish peroxidase (HRP). HRP converts H_2O_2 into •OH. The latter oxidizes TMB, converting it to a blue oxidized product, and peaks at 370 nm and 652 nm can be seen in the UV-vis spectrum. Spectra for a $CoFe_2O_4$@PSiC-KCN/ultrasound treated glucose solution and controls are given in Fig. 2C, clearly showing that the piezoelectric catalysis had generated H_2O_2. The catalytic activity of $CoFe_2O_4$@PSiC-KCN was found to be affected by pH, and maximized at pH = 3 (Fig. 2D). An acidic environment hence makes $CoFe_2O_4$@PSiC-KCN more effective in catalyzing the breakdown of glucose, which given the acidic TME is potentially beneficial for the material if it us to be used to treat tumors.

The enzymatic reaction rate was explored as a function of concentration for both $CoFe_2O_4$@PSiC-KCN and GOx (Fig. 2E). The catalytic rate of $CoFe_2O_4$@PSiC-KCN was found to be high: a NP concentration of 0.64 mg/mL performed better than 2.5 μg/mL of GOx.

If $CoFe_2O_4$@PSiC-KCN or H_2O_2 are separately combined with TMB, there are no changes seen in the UV-vis spectrum (Fig. 2F), indicating that TMB cannot be oxidized under these conditions. However, if $CoFe_2O_4$@PSiC-KCN and hydrogen peroxide together are mixed with TMB solution, peaks at 370 nm and 552 nm appear even without HRP. This is because $CoFe_2O_4$@PSiC-KCN directly catalyzes H_2O_2 to produce •OH, and TMB is oxidized by •OH to obtain a blue product. These findings thus demonstrate that $CoFe_2O_4$@PSiC nanoparticles can catalyze H_2O_2 to produce free radicals to kill tumors (Fig. 2F). As shown in Fig. 2G, the optimal pH for this process is 3.

When $CoFe_2O_4$@PSiC-KCN is loaded in a glucose solution containing TMB and HRP, the UV-vis spectrum of the reaction solution under ultrasound reveals TMB oxidation peaks at 370 nm and 552 nm, and the solution turns blue (Fig. S8A). This indicates that the material has the ability to catalyze the production of H_2O_2 from glucose under ultrasound. In addition to UV spectrophotometry, the production of ROS was detected using electron-spin resonance (ESR) spectroscopy. The presence of characteristic absorbance peaks of the marker DMPO–•OH substantiate the presence of •OH[34]. There was nearly no HO• generation in a

suspension of $CoFe_2O_4$@PSiC-KCN in glucose solution. However, the application of US irradiation notably enhances the absorption peak intensity in the $CoFe_2O_4$@PSiC-KCN + 100 mM glucose + US group compared to the group without ultrasound (Fig. S8B). This clearly evidences the production of ·OH.

The enzyme-mimetic kinetics were quantified using the Michaelis-Menten model. The Michaelis constant was determined using $V = V_{max}[S]/(K_m + [S])$, where V is the initial velocity, $[S]$ is the concentration of the substrate, K_m is the Michaelis constant, and V_{max} is maximum velocity of reaction for the enzyme concentration employed. Plots are shown in Figure S9. When fixing the H_2O_2 concentration, the V_{max} of $CoFe_2O_4$@$PSiO_2$-KCN and HRP are 6.7240×10^{-3} and 5.1673×10^{-9} M/s, respectively. The K_m value of $CoFe_2O_4$@$PSiO_2$-KCN is lower than that of HRP, indicating that the affinity between $CoFe_2O_4$@PSiC-KCN and TMB is lower (Fig. S9A, C). When fixing the TMB concentration, the V_{max} of and HRP are 5.3630×10^{-3} and 2.2260×10^{-8} M/s, respectively. Here, the K_m value of $CoFe_2O_4$@PSiC-KCN is again lower than that of HRP (Fig. S9B, D).

These data clearly show that $CoFe_2O_4$@PSiC-KCN is able to achieve both glucose oxidation and peroxidase mimetic properties, both of which are enhanced under acidic conditions. The findings thus suggest that the system could have potent cancer cell killing abilities in the acidic TME (Fig. 2H).

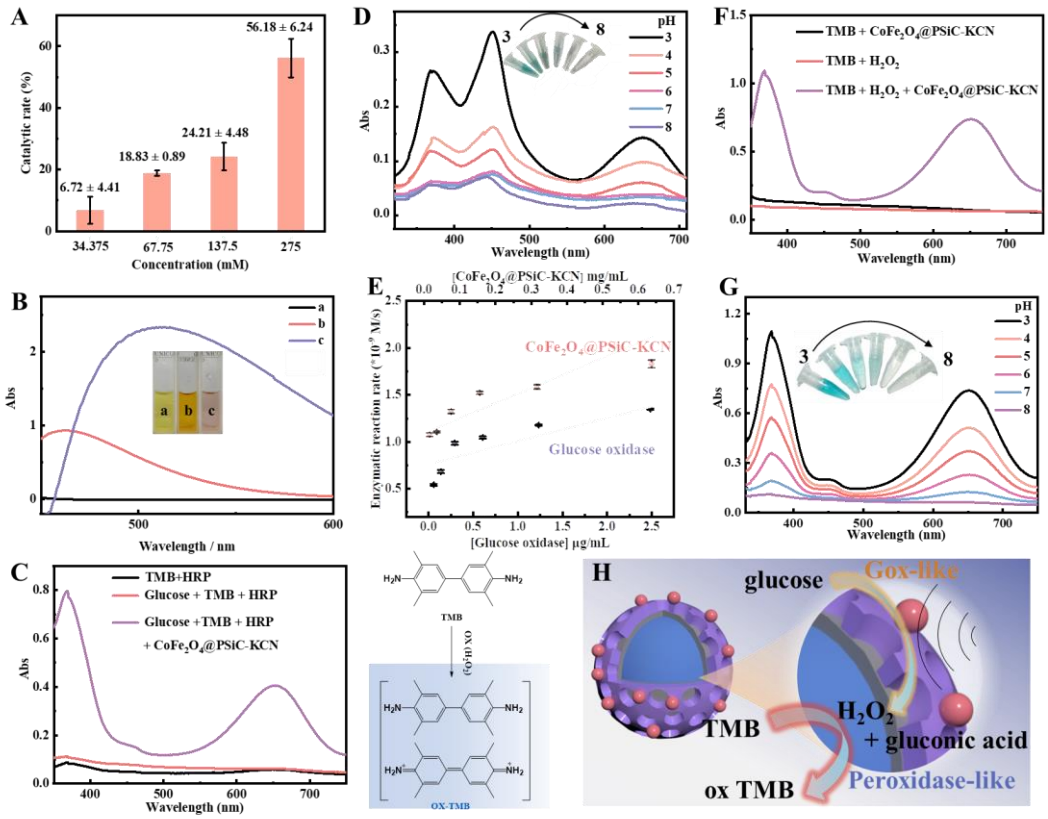

Figure 2 Exploration of the catalytic properties of the $CoFe_2O_4$@PSiC-KCN NPs. (A) Glucose degradation rate as a function of NP concentration. (B) Confirmation of gluconic acid production using hydroxylamine and Fe^{3+} colorimetry; curves correspond to (a) glucose solution alone; (b) $CoFe_2O_4$@PSiC-KCN suspension;

(c) glucose solution + $CoFe_2O_4$@PSiC-KCN. TMB assay results (C) either with or without the presence of $CoFe_2O_4$@PSiC-KCN. (D) in the presence of $CoFe_2O_4$@PSiC-KCN and at different pH values. (E) A comparison of GOx and $CoFe_2O_4$@PSiC-KCN catalytic properties in the presence of different concentrations of glucose. UV-vis absorption spectra of glucose solutions combined with TMB and H_2O_2. (F) either with or without the presence of $CoFe_2O_4$@PSiC-KCN. (G) in the presence of $CoFe_2O_4$@PSiC-KCN and at different pH values. (H) Schematic diagram illustrating the $CoFe_2O_4$@PSiC-KCN cascade catalytic system.

2.3 Uptake and cytotoxicity

$CoFe_2O_4$@PSiC-KCN must be able to enter cells in order to exert a cytotoxic effect. To explore this, $CoFe_2O_4$@PSiC-KCN was labeled with Rhodamine (Rho) through EDC coupling, and the uptake of the tagged material by 4T1 cells was observed by confocal laser scanning microscope (CLSM). Over 24 h, $CoFe_2O_4$@PSiC-KCN-Rho is effectively taken up by cells (Fig. 3A), as evidenced by increasingly noticeable red fluorescence inside the cells with time (Fig. 3B). Uptake appears to be slightly enhanced when the cells are also treated with ultrasound (US) (Fig. 3A, B; Fig. S10). Ultrasound can damage the cell membrane, thereby increasing the uptake of nanomaterials by 4T1 cells.[35] This is consistent with the literature[36]. The fluorescence is distributed in the cytoplasm of 4T1 cells.

The cytotoxicity and biocompatibility of the NPs was next studied by the MTT method. First, we performed a cytocompatibility evaluation of the NPs, using the C2C12 muscle precursor cell line. Fig. 3C shows the relative cell viability of C2C12 cells after co-incubation with $CoFe_2O_4$@PSiC-KCN for 24 h. It can be seen that even if the sum of the Fe and Co concentrations ([Co+Fe]) was as high as 55.71 μg/mL, the viability of the cells remained above 91%, demonstrating high cytocompatibility.

Next, we investigated the effect of various formulations on cancerous 4T1 cells (Fig. 3D). Here, marked cytotoxicity can be observed. The most intuitive reason for this is that the acidic environment of tumor cells facilitates the catalytic effects of NPs. We further investigated the cytotoxicity of the NPs at different concentrations of Ber or [Co+Fe] and with a US treatment (Fig. 3D). The results showed a Ber/[Co+Fe] concentration-dependent cytotoxicity. It can be seen that $CoFe_2O_4$@PSiC-KCN is much more lethal than free Ber and $CoFe_2O_4$@PSiC to 4T1. When the concentration of Ber is 1.0 μg/mL or [Co+Fe] = 55.71 μg/mL, the survival rates of 4T1 cells treated with free Ber, $CoFe_2O_4$@PSiC NPs, $CoFe_2O_4$@PSiC-KCN and Ber/$CoFe_2O_4$@PSiC-KCN decreased to 58.98%, 41.83%, 24.04%, and 17.66% respectively after 24 h of treatment and a 60 s US exposure. The survival rate of Ber/$CoFe_2O_4$@PSiC-KCN cells in the combined treatment group was significantly lower than those in the single treatment groups.

Quantitative analysis of cell apoptosis was performed using flow cytometry and Annexin V-EGFP and PI staining of 4T1 cells (Fig. S11). The early apoptosis, late apoptosis, and necrosis rates of cells in the control

group treated with PBS were 0.065%, 0.086%, and 0.14%, respectively. These increased somewhat when cells were given PBS + US (to 0.6%, 6.0%, and 6.2%), indicating the role of US in promoting cell apoptosis. Under US stimulation, the total (early + late) apoptosis rates of the free Ber (lactate accumulation), KCN (glucose consumption and H_2O_2 production), and $CoFe_2O_4$@PSiC group (consuming H_2O_2 to produce ROS) were 36.5%, 36.7%, and 41.0%, respectively. The early (10.3%) and late (40.5%) apoptosis rates of cells in the Ber/$CoFe_2O_4$@PSiC-KCN+US group were the highest, demonstrating the synergistic effect of acid accumulation, glucose consumption, and increased H_2O_2 levels.

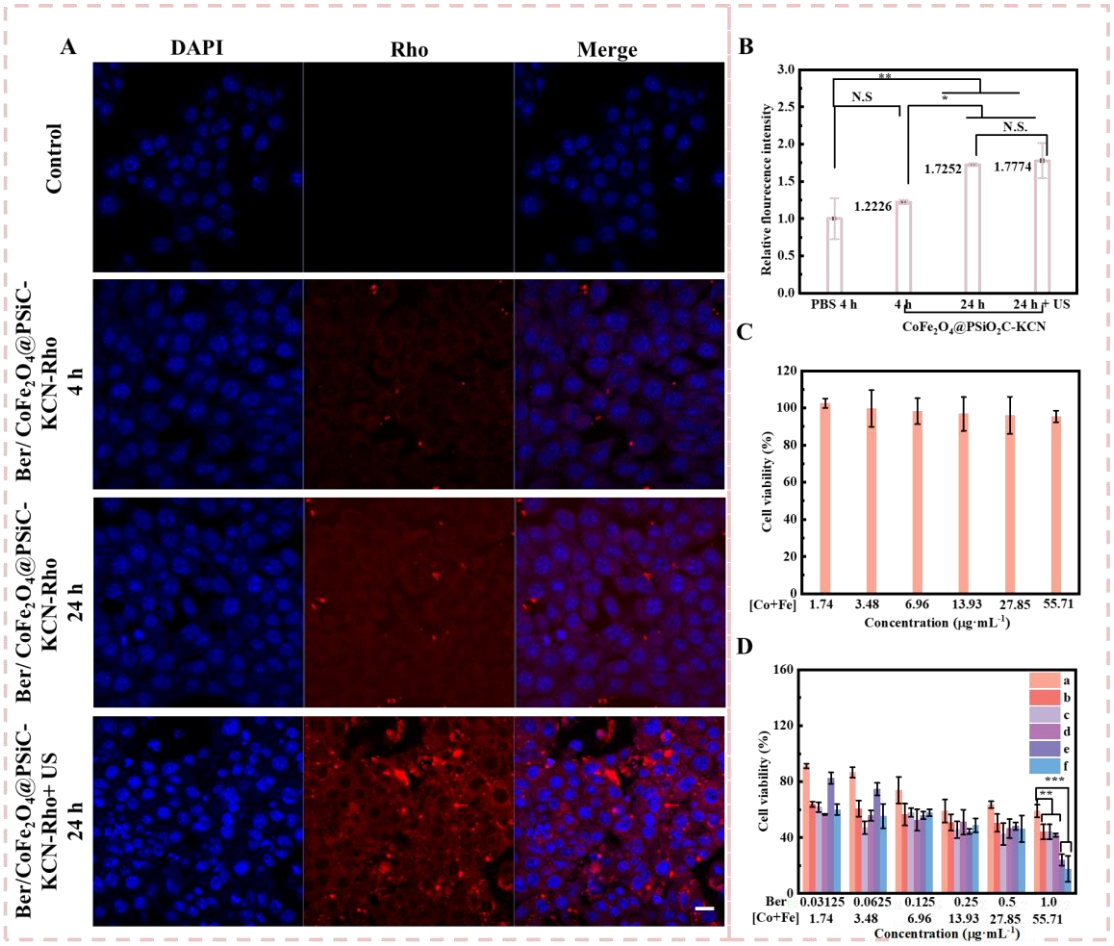

Figure 3 Intracellular delivery and anticancer effects of $CoFe_2O_4$@PSiC-KCN. (A) Representative CLSM images of 4T1 cells incubated with $CoFe_2O_4$@PSiC-KCN-Rho suspension for various time periods, with and without US. (B) Relative intracellular fluorescence intensity measured by flow cytometry. (C) Viability of C2C12 cells treated with $CoFe_2O_4$@PSiC-KCN. (D) 4T1 cells treated with (a) free Ber + US, (b) KCN + US, (c) $CoFe_2O_4$ + US, (d) $CoFe_2O_4$@PSiC + US, (E) $CoFe_2O_4$@PSiC-KCN + US, (f) Ber/$CoFe_2O_4$@PSiC-KCN + US (1.0 w·cm^{-2}, 60 s). The data are displayed as mean ± S.D. (n=3). (N.S.: not significant, * P<0.05, * * P<0.01, and * * * P<0.001). Scale bars: 20 μm.

2.4 Mechanism of therapeutic action

The next series of experiments performed sought to understand the mechanism of action of the Ber/$CoFe_2O_4$@PSiC-KCN system. It is known that inhibition of the activity of mitochondrial complex I in cells increases lactate levels[31], and previous studies have shown that Ber can inhibit mitochondrial complex I[32] and hence should lead to lactate accumulation (Fig. 4A). We sought to verify whether Ber/$CoFe_2O_4$@PSiC-KCN can cause lactate accumulation *in vitro*. Fig. 4B shows that free Ber (0.18 μg/mL) can increase the amount of lactate in tumor cells by 1.74-fold. In Ber/$CoFe_2O_4$@PSiC-KCN, the drug appears to play a similar role, in a concentration-dependent manner: the higher the concentration, the more lactic acid accumulates. The accumulation of lactic acid leads to a more acidic environment in the cells[37], which accelerates the Fenton reaction. This will acidify the TME, enhancing the efficacy of CDT.[38, 39]

KCN can catalyze glucose and produce hydrogen peroxide through piezoelectric catalysis. To verify this, intracellular glucose was measured. Under ultrasound, both KCN and $CoFe_2O_4$@PSiC-KCN can significantly reduce the intracellular glucose concentration (Fig. S12A), indicating that KCN can catalyze glucose degradation. A MTT experiment can also indirectly demonstrate that the material catalyzes intracellular glucose degradation, and the product is toxic to cells. The concentration-related cell killing ability of Ber/$CoFe_2O_4$@PSiC-KCN was evaluated in media with/without glucose. Cell viability when incubated in the glucose-supplemented medium with Ber/$CoFe_2O_4$@PSiC-KCN was notably lower than the non-glucose-supplemented medium (Fig. S12B), indicating that the glucose-triggered cascade catalytic reaction could effectively generate ·OH for killing cancer cells.

A second reason for the toxic effect of Ber/$CoFe_2O_4$@PSiC-KCN on tumor cells is expected to be the CDT that catalyzes the production of ROS through Fenton reactions, and leads to ferroptosis caused by GSH consumption. The 2',7'-dichlorofluorescein diacetate (DCFH-DA) probe was used to stain 4T1 cells to reveal the presence of intracellular ROS. Flow cytometry results are presented in Fig. 4C. The $CoFe_2O_4$@PSiC NPs can produce some ROS due to the endogenous H_2O_2 inside tumor cells. Ber/$CoFe_2O_4$@PSiC-KCN produces more ROS than $CoFe_2O_4$@PSiC, and this increases with increasing NP concentration. The fluorescence signal intensity of the DCFH-DA probe was also assessed by imaging. It was found that there was almost no fluorescence in the control group (Fig. S13). As the concentration of Ber/ $CoFe_2O_4$@PSiC-KCN increases, the fluorescence signal gradually enhances, indicating an increase in intracellular ROS production. This is expected to be because Ber/$CoFe_2O_4$@PSiC-KCN catalyzes the reaction of glucose to produce H_2O_2, and then the conversion of H_2O_2 to ·OH radicals, thereby supplementing the natural abundance of H_2O_2.

Glutathione is responsible for maintaining the redox balance within tumor cells. In ferroptosis, reduced glutathione (GSH) is consumed, which renders it unable to convert lipid hydroperoxide into non-toxic lipid alcohol.[40] When the concentration of ROS increases in cells, GSH is depleted, which reduces the intracellular GSH/ glutathione disulfide (GSSG) ratio. This ratio can be measured and used to gain some insight into

ferroptosis. The GSH/GSSG ratio (Fig. 4D) sharply decreased from 68.86% when cells were treated with US only, to 18.39% with Ber/$CoFe_2O_4$@PSiC-KCN + US (30 μg·mL^{-1}). Hence, it appears that the NPs are able to drive the ferroptosis mechanism of cell death. Ber/$CoFe_2O_4$@PSiC-KCN can hence kill tumor cells through the above mechanisms. In addition to ferroptosis, Ber/$CoFe_2O_4$@PSiC-KCN can also affect the mitochondrial membrane potential of tumor cells. Both Ber and $CoFe_2O_4$@PSiC can reduce mitochondrial membrane potential and have a synergistic effect (Fig. S14). When cell death happens, tumor cells can generate damage related molecular patterns (DAMPs) which are expected in turn to induce ICD. Several common DAMPs are the presence of extracellular adenosine triphosphate (ATP), HMGB-1 and CRT. To investigate whether the NPs can lead to ICD, the amount of ATP released from cells was quantified. Compared with a control group treated with US alone, Ber/$CoFe_2O_4$@PSiC-KCN + US led to a significant increase in extracellular ATP (Fig. S15A), from 7.68 mM to 11.36 mM. The Ber/$CoFe_2O_4$@PSiC-KCN +US group also promoted the release of HMGB-1 and CRT to a some extent, to 1.28 and 1.06-fold of the value see with a control US treatment (Fig. S15B). This is indicative that DAMPs are generated via the CDT-induced cell death caused by the NPs, and thus that they can cause ICD as an additional mechanism of tumor destruction.

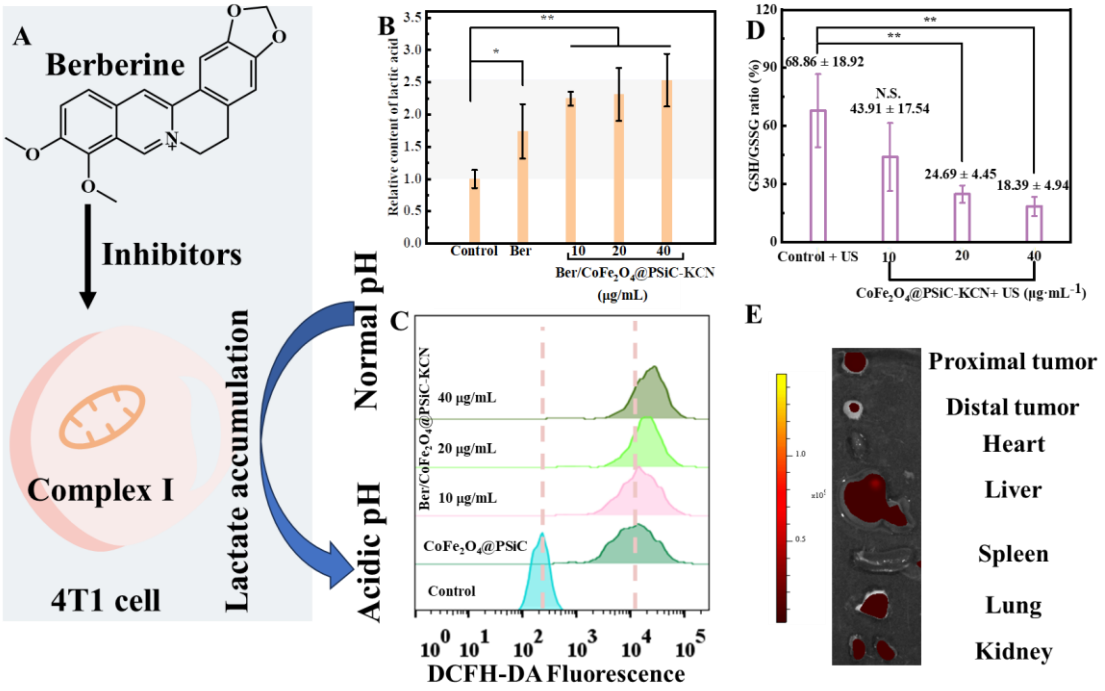

Figure 4 Mechanism of therapeutic action. (A) Ber increases lactate accumulation in tumors by inhibiting mitochondrial complex I. (B) Detection of intracellular lactate content relative to a control (no treatment) in 4T1 cells treated with different formulations (Ber concentration: 0.18 μg/mL and given a US treatment for 60 s). (C) The results of assays using DCFH-DA as a probe for •OH detection in cells incubated with different

NPs (and given a US treatment for 60 s). (D) Detection of the intracellular GSH/GSSG ratio in 4T1 cells treated with different NPs. (E) The distribution of $CoFe_2O_4$@PSiC-KCN-ICG in mouse tissues. Red represents the fluorescence emitted by Ber/$CoFe_2O_4$@PSiC-KCN-ICG. The data are displayed as mean ± S.D. (n=3) Three independent experiments were performed, with five replicate wells per experiment. (N.S.: not significant, * P<0.05, * * P<0.01, and * * * P<0.001).

2.5 Cell migration

The extent of 4T1 cell migration is related to a tumor's metastatic potential: the further the cells can migrate, the greater this potential is. This can be assessed *in vitro* with a simple scratch assay (see Fig. S16). Over 48 h period, cells are clearly moving across the scratch area both with a control group (PBS) and US and cells treated with Ber/$CoFe_2O_4$@PSiC-KCN+US. However, cell mobility in the latter case was significantly reduced, with migration rates of 8.2 and 17.3% at 24 h and 48 h (cf. 24.0 and 37.8 with PBS), respectively. The NPs thus markedly reduce cell migration. These experiments were conducted using NP concentrations observed not to cause appreciable cytotoxicity, and thus cell death is not likely to be the cause of this observation.

2.6 Blood compatibility analysis

Evaluating hemolytic activity is vital to ensure that prospective medicines will not cause damage upon administration. Assays were thus performed to determine the compatibility of the NP formulations with red blood cells (Fig. S17). The results showed that after 1 hour, 0.5 mg/mL Ber showed only 1.5% hemolytic activity, comparable to the negative control. According to ASTM standards, these values are within the acceptable range of 5%[41]. There is also no noticeable change in the cell morphology after exposure of red blood cells to the NPs (see Fig. S17). Therefore, it appears that the Ber/$CoFe_2O_4$@PSiC-KCN NPs could be suitable for *in vivo* administration.

2.7 *In vivo* imaging and distribution

Indocyanin green (ICG) labeled Ber/$CoFe_2O_4$@PSiC-KCN NPs were used to explore the particle distribution in mice. The results are shown in Fig. S18. After peritumoral injection, the material showed significant signal enhancement in the proximal tumor at 2-6 h. The distal tumor also demonstrated evidence of NP ingress owing to their circulation and transport in the blood. The fluorescence signal of the material gradually weakened after 6-24 h. These results indicate that the NPs will gradually enter the proximal tumor site to exert therapeutic effects, and this reaches a maximum 6 hours after injection. A small amount of

material will enter the distal tumor via the blood circulation, and thus the NPs can potentially have therapeutic effects here also.

$CoFe_2O_4$ has been proven to have T2-weighted magnetic resonance imaging performance[42]. We thus studied the MR imaging properties of Ber/$CoFe_2O_4$@PSiC-KCN NPs and found that in aqueous suspsension the MR signal intensity increased in a concentration dependent manner with [Co+Fe] (Fig. S19A). In a 4T1 tumor model when Ber/$CoFe_2O_4$@PSiC-KCN NPs was administered through proximal tumor peritumoral injection, the strongest MR signal was observed 6 h after injection. There is clear signal enhancement at both the proximal and distal tumor sites. These results are consistent with the fluorescence date, and together both indicate that Ber/$CoFe_2O_4$@PSiC-KCN NPs can accumulate in both the proximal and distal tumor regions, helping to maintain the anticancer effect of tumor site particles and visualize treatment.

2.8 Antitumor efficacy *in vivo*

A bilateral 4T1 tumor model was constructed (Fig. 5A) to examine the therapeutic efficacy of Ber/$CoFe_2O_4$@PSiC-KCN *in vivo*. Mice were treated six times with the following formulations, every two days: (a) PBS; (b) Ber; (c) KCN; (d) $CoFe_2O_4$@PSiC; (e) $CoFe_2O_4$@PSiC-KCN; and (f) Ber/$CoFe_2O_4$@PSiC-KCN. 6 h after peritumoral injection of the proximal tumor, the proximal tumor was exposed to US irradiation. During the treatment period, there were no significant weight changes of the mice in any of the groups, indicating negligible systemic toxicity (Fig. 5B, Fig. S20). The primary tumors of mice treated only with PBS and $CoFe_2O_4$@PSiC were found to grow very quickly (Fig. 5C), with volumes by day 12 being 9.03 and 7.41 times that of day 0, respectively. The group with the best therapeutic effect has inhibition rates of 82.0% and 78.7% for the proximal and distal tumors, respectively (Fig. S21). It indicated that these have poor anti-tumor effects, and the chemodynamic therapy delivered by $CoFe_2O_4$@PSiC alone is not effective. Ber/$CoFe_2O_4$@PSiC-KCN has the best therapeutic effect on the proximal tumors, with slight growth noted during the experimental period. Compared with the phosphate responsive nanoparticles of metal organic frameworks that are also beneficial for hunger-chemodynamic therapy, this work has a better therapeutic effect on tumors[43]. Ber, KCN and $CoFe_2O_4$@PSiC-KCN have varied but intermediate activity. Considering the distal tumors (Fig. 5D), the differences between the treatment groups are smaller. However, the PBS treatment still leads to the largest tumors, and there is no notable growth seen with Ber/$CoFe_2O_4$@PSiC-KCN. This can be attributed to the muti-faceted tumor therapy provided by the latter.

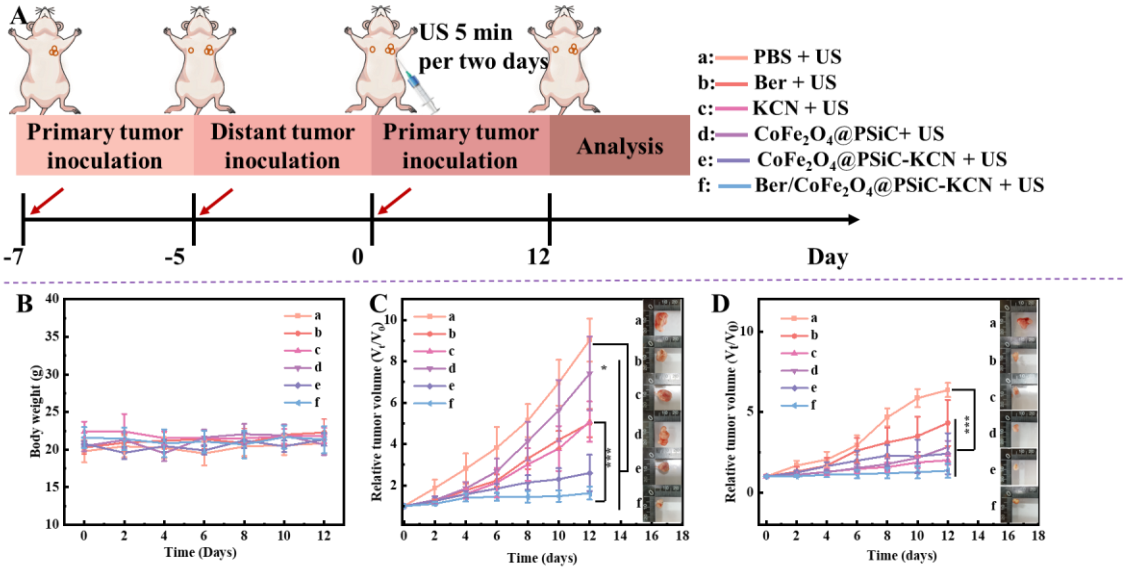

Figure 5 *In vivo* anti-tumor efficacy in a murine bilateral 4T1 tumor model. (A) The *in vivo* anti-tumor treatment plan. 4T1 cells were inoculated into the proximal left and distal right armpits of BALB/c mice on days -7 and -5, respectively. On day zero and every two days thereafter, the mice were subcutaneously injected with various formulations into the proximal tumor. Treatment groups are as follows: (a) PBS + US; (b) free Ber + US; (c) KCN + US; (d) $CoFe_2O_4$@PSiC + US; (e) $CoFe_2O_4$@PSiC-KCN + US; (f) Ber/$CoFe_2O_4$@PSiC-KCN + US. Primary tumor ultrasound was performed for 5 minutes 6 hours after each injection. (B) Body weights during the experimental period. (C) Relative tumor-growth curves as a function of time are shown for primary tumors. (D) Relative tumor-growth curves as a function of time are shown for distal tumors.

We next investigated the mechanism underpinning the NPs' tumor-killing ability. There is a large amount of ROS present in the tumor tissue after treatment with Ber/$CoFe_2O_4$@PSiC-KCN + US (Fig. S22). Materials containing Fe(Ⅱ/Ⅲ) and Cu (Ⅱ) generate ROS through Fenton reactions, leading to intracellular redox imbalance and inducing downregulation of GPX4, indirectly leading to LPO accumulation.[44, 45] The Ber/$CoFe_2O_4$@PSiC-KCN group showed downregulation of the lipid peroxidation regulation enzyme glutathione peroxidase-4 (GPX4, (Fig. 6A), which is supportive of ferroptosis being involved in the cell death process. Staining was also performed to assess lipid peroxidation (LPO). In this, a brown-yellow color represents a high concentration of LPO antigen. The results (Fig. 6B) showed that the expression levels of LPO in the KCN + US, $CoFe_2O_4$@PSiC-KCN + US and Ber/$CoFe_2O_4$@PSiC-KCN + US groups were higher than those in the PBS + US control group (Fig. 6B, Fig. S23). The ROS generated by the Ber/$CoFe_2O_4$@PSiC-KCN + US group leads to downregulation of GPX4 and accumulation of LPO. LPO accumulation ultimately leads to ferroptosis.[46] This suggests that KCN and Ber in the formulations can enhance ferroptosis and thus improve anti-tumor efficacy.

The accumulation of ROS generated by the presence of NPs in the tumor tissue can cause ICD of tumor cells. A key characteristic of ICD is the release of damage related patterns (DAMPs). Typical DAMP markers were thus assessed. Calreticulin (CRT) has been proven to be a key diagnostic for ICD,[47] while high mobility group box 1 (HMGB1) protein is also known to be released by dying tumor cells. The abundance of these species can thus provide some insight into the extent of ICD. Compared with the PBS+US control group, the Ber/$CoFe_2O_4$@PSiC-KCN treatment group showed an increase in the release of CRT and HMGB1, suggesting the involvement of ICD (Fig. 6A, B). This is conducive to subsequent DC maturation and T cell activation.

In the H&E section of the proximal tumor Ber treatment group, the arrangement of nuclei became sparse after treatment, and the red blood cell proliferation markers (Ki67, red) in this group were reduced compared to the PBS group. Both H&E and Ki67 staining confirmed that the most extensive cell apoptosis in the proximal tumor is seen with the Ber/$CoFe_2O_4$@PSiC-KCN+US group (Fig. 6B, Fig. S24 and Fig. S25). The distal tumors exhibit the same trend as the proximal tumors, indicating that Ber/$CoFe_2O_4$@PSiC-KCN also has therapeutic effects here (Fig. S25). The tumor tissues were also evaluated for necrosis and apoptosis using terminal deoxynucleotidyl transferase-mediated dUTP-biotin nick end labelling (TUNEL) staining. Yellow color in the slices indicates apoptosis of tumor cells. The TUNEL data show the greatest degree of apoptosis in the Ber/$CoFe_2O_4$@PSiC-KCN+US group, as can be seen from the increased presence of yellow in the images (Fig. S26). Representative H&E staining images (Fig. 6C) of lung tissue clearly indicate that the number and size of visible metastatic nodules are reduced after Ber/$CoFe_2O_4$@PSiC-KCN treatment, indicating that the material has a certain degree of anti-tumor metastasis properties.

The possibility for ICD was also explored in terms of lymphocyte recruitment (Fig. S27-S28, Fig. 6D). Fig. 6D shows the content of cytokines in the Ber/ $CoFe_2O_4$@PSiC-KCN + US treated tissue relative to the PBS+US group. The surface markers CD86, CD3, and CD8 (typical markers for macrophages and T-cells) were probed, and it was found that at both the proximal and distal tumor sites there was elevated presence of these markers post-treatment with Ber/$CoFe_2O_4$@PSiC-KCN + US, indicating the ability of the NPs to stimulate ICD. Inflammatory factors IL-6 and chemokines TNF- α increased by 20% and 287% respectively, and the length of the spleen is closer to normal in the Ber/$CoFe_2O_4$@PSiC-KCN + US group (Fig. 6D). The spleen of the Ber/$CoFe_2O_4$@PSiC-KCN + US treatment group is smaller than that of the PBS + US group and closer to the normal state of the spleen.

The presence of Co in the tumors was next investigated (Fig. 6E). As expected, no Co was detected in mice treated with PBS, Ber or KCN and ultrasound. In contrast, when the mice were given $CoFe_2O_4$@PSiC+ US, $CoFe_2O_4$@PSiC-KCN + US, or Ber/ $CoFe_2O_4$@PSiC-KCN + US, high levels of Co can be found in the proximal tumor. Co is also detected, albeit to a lesser extent, in the distal tumors in all three of the latter groups. This demonstrates that the NPs are transported to the distal tumor even after proximal injection, and permits them to have therapeutic effect outside the immediate injection area.

2.9 Biosafety analysis

H&E staining and blood serum analyses were undertaken to determine the *in vivo* biocompatibility of the formulations. No metastasis was found in the main organs of the heart, liver, spleen, and kidney (Fig. S29), and all appeared to be healthy. By detecting the contents of the biomarkers alanine transaminase (ALT), aspartate aminotransferase (AST), creatinine (CRE) and blood urea nitrogen (BUN) in serum, we investigated whether the materials cause any systemic toxicity to mice. ALT, AST, CRE and BUN levels in the serum of mice after treatment were not significantly different from those in the PBS + US group (Fig. 6F). These results confirm that there appear not to be any off-target side effects from treatment with Ber/$CoFe_2O_4$@PSiC-KCN, and thus that the systems could potentially be used for cancer therapy.

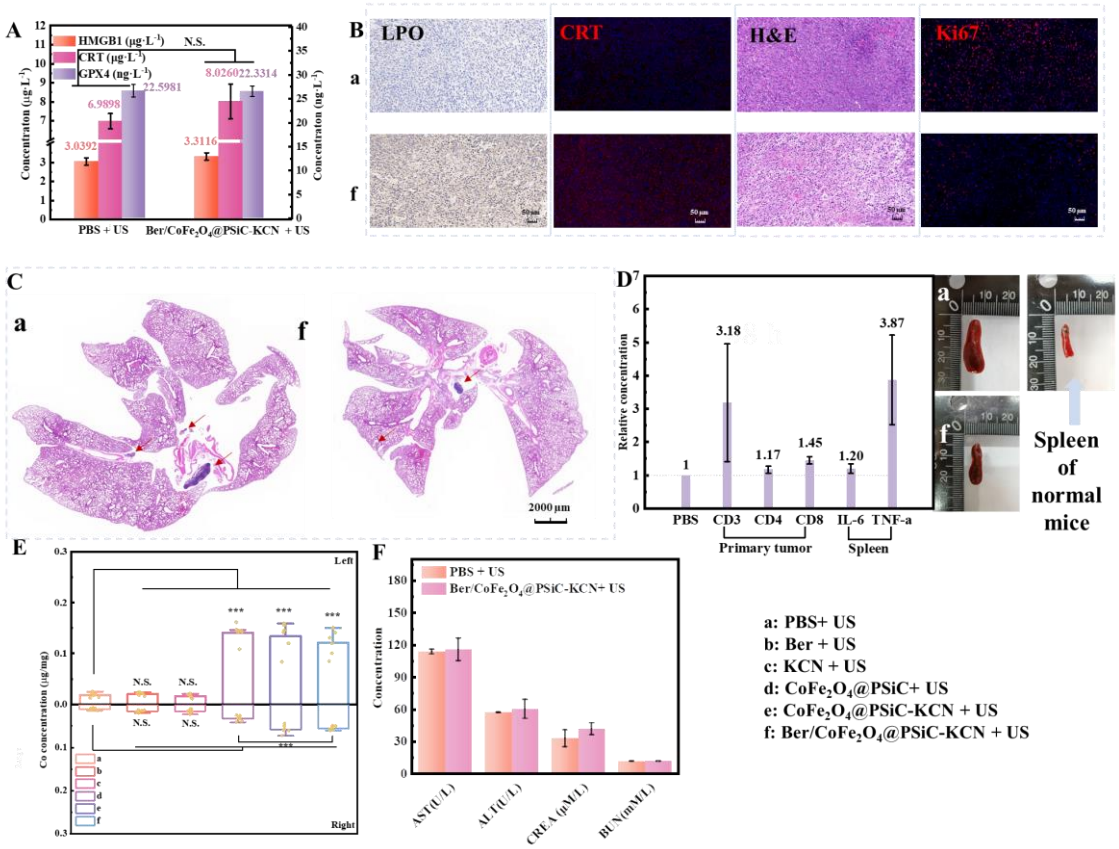

Figure 6 Ex vivo analysis of murine tissue after various treatments. (A) Determination of HMGB1, CRT and GPX4 content in the tumor tissues after treatment. (B) CRT, LPO, H&E, and Ki67 staining of tumor tissues collected from different treatment groups. (C) H&E staining of lung tissues from mice either treated with PBS or Ber/$CoFe_2O_4$@PSiC-KCN. (D) Analysis of the relative content of CD3, CD4, CD8 in the tumor tissue and IL-6 and TNF-α in the spleen after treatment with Ber/$CoFe_2O_4$@PSiC-KCN + US or PBS + US, with photos of spleen tissue. (E) Analysis of Co content in the proximal (left) and distal (right) tumors after

treatment. (F) Analysis of blood biochemical indicators.

Multi metal composite nanoparticles have previously been reported to enhance Fenton reactions through heterogeneity/loop synergy to promote the use of ·OH[48, 49] in CDT. However, this method still demands high levels of H_2O_2 and favorable pH, which are typically not present in tumors. In this work, the Ber/$CoFe_2O_4$@PSiC-KCN system has a cascading catalytic ability, with KCN first converting glucose molecules into H_2O_2, and then $CoFe_2O_4$ generating ·OH from the H_2O_2. Ber drives the accumulation of lactic acid in the tumor, providing a more acidic environment that is conducive to the Fenton reaction. This supplements the local endogenous H_2O_2 content, thus increasing the efficacy of treatment. Compared to expensive precious metals used in previous work[50, 51] to provide glucose catalytic functions, the system reported here uses cheap and readily obtained materials, thus permitting a more cost-effective intervention to be put in place.

3 Conclusion

In this work we have developed a novel piezoelectric cascade catalyst for the treatment of cancer. $CoFe_2O_4$ NPs were prepared, coated with silica, and then functionalized with the piezoelectric response material KCN and loaded with the drug Ber. The resultant Ber/$CoFe_2O_4$@PSiC-KCN system can both catalase the conversion of glucose into gluconic acid and H_2O_2 and also the reaction of the latter to form ·OH radicals. The latter can provide chemodynamic therapy, while also reducing GSH levels and leading to ferroptosis. In addition, the presence of Ber helps to acidify the local environment, accelerating these effects. The resultant cell death leads to the promotion of damage-associated molecular patterns and thus to ICD. The particles are readily taken up by cancer cells *in vitro*, and when combined with an ultrasound (US) treatment leading to much increased cell death. In a murine *in vivo* bilateral tumor model, Ber/$CoFe_2O_4$@PSiC-KCN is found to significantly inhibit both proximal and distal tumor growth, and protects the lungs from tumor metastasis. Immune cell recruitment to the tumors is clearly visible from ex vivo staining experiments, and there is no off-target toxicity noted. This work thus proposes a new strategy for piezoelectric response-activated combined anti-cancer therapy, which has the potential for clinical application.

Resource availability

Lead contact

Further information and requests for materials should be directed to and will be fulfilled by the lead contact, Li-Min Zhu (lzhu@dhu.edu.cn).

Materials availability

The materials generated in this study are available from the corresponding author upon request.

Data and code availability

The data used to support the findings of this study are available from the corresponding author upon request.

Supporting Information

The Supporting Information is available free of charge at xxx.

Acknowledgements

This work was supported by the Science and Technology Commission of Shanghai Municipality [grant numbers 22520710400, 21WZ2501300, 20DZ2254900]; the Biomedical Textile Materials “111 Project” of the Ministry of Education of China [grant number B07024]; the Young Scientists Fund of the National Natural Science Foundation of China [grant number 82104403]; the Special Fund for Science and Technology Innovation of Shanghai Jiao Tong University [project no. YG2019ZDA27]; and the Natural Science Foundation of Shanghai [project No. 20ZR1444600].

Author contributions

Conceptualization, Y.L.Z. and L.Z.; Methodology, Y.L.Z. and L.Z; Investigation, Y.L.Z., Y.Z., W.T., Y.Y.Z., and J.X; Writing – Original Draft, Y.L.Z.; Writing – Review & Editing, Y.D., Y.L.Z., G.W., and L.Z.; Funding Acquisition, L.Z. and F.L. and J.W.; Resources, L.Z. and F.L. and J.W.; All authors proofread, commented on, and approved the final version of the manuscript.

Declaration of interests: The authors declare no competing interests.

References

[1] S. Hui, J. M. Ghergurovich, R. J. Morscher, C. Jang, X. Teng, W. Lu, L. A. Esparza, T. Reya, Z. Le, J. Yanxiang Guo, E. White, J. D. Rabinowitz, Glucose feeds the tca cycle via circulating lactate, Nature. 551 (2017) 115-118. https://doi.org/10.1038/nature24057

[2] R. Fan, C. Chen, J. Hu, M. Mu, D. Chuan, Z. Chen, G. Guo, J. Xu, Multifunctional gold nanorods in low-temperature photothermal interactions for combined tumor starvation and rna interference therapy, Acta Biomater. 159 (2023) 324-337. https://doi.org/10.1016/j.actbio.2023.01.036

[3] M. Sun, M. Yang, S. Li, C. Wang, F. Zhang, B. Xu, Y. Zhang, X. Sun, Q. Yuan, H. Liu, Photothermal lysis of engineered bacteria to modulate amino acid metabolism against tumors, Adv. Funct. Mater. 33 (2023) 2212226. https://doi.org/10.1002/adfm.202212226

[4] F. Duan, W. Jin, T. Zhang, Y. Sun, X. Deng, W. Gao, Thermo-ph-sensitive polymer conjugated glucose oxidase for tumour-selective starvation-oxidation-immune therapy, Adv. Mater. 20 (2023) 2209765. https://doi.org/10.1002/adma.202209765

[5] S. Paul, S. Ghosh, S. Kumar, Tumor glycolysis, an essential sweet tooth of tumor cells, Semin. Cancer Biol. 86 (2022) 1216-1230. https://doi.org/10.1016/j.semcancer.2022.09.007

[6] J. Yu, B. Shao, M. Luo, W. Du, W. Nie, J. Yang, X. Wei, Irradiated lactic acid-stimulated tumour cells promote the antitumour immunity as a therapeutic vaccine, Cancer Lett. 469 (2020) 367-379. https://doi.org/10.1016/j.canlet.2019.11.018

[7] Q. Feng, Z. Liu, X. Yu, T. Huang, J. Chen, J. Wang, J. Wilhelm, S. Li, J. Song, W. Li, Z. Sun, B. D. Sumer, B. Li, Y.-X. Fu, J. Gao, Lactate increases stemness of cd8 + t cells to augment anti-tumor immunity, Nat. Commun. 13 (2022) 4981. https://doi.org/10.1038/s41467-022-32521-8

[8] Y. Li, Y. Zhang, Y. Dong, O. U. Akakuru, X. Yao, J. Yi, X. Li, L. Wang, X. Lou, B. Zhu, K. Fan, Z. Qin, Ablation of gap junction protein improves the efficiency of nanozyme-mediated catalytic/starvation/mild-temperature photothermal therapy, Adv. Mater. 35 (2023) 2210464. https://doi.org/10.1002/adma.202210464

[9] M. Li, X. Luo, S. Lei, Y. Liu, H. Guo, Y. Zhang, Y. Pan, K. Chen, J. Lin, P. Huang, Synchronous interventions of glucose and mitochondrial metabolisms for antitumor bioenergetic therapy, Adv. Mater. 35 (2023) 2301099. https://doi.org/10.1002/adma.202301099

[10] W. Wang, R. Jia, F. Qu, H. Lin, Defect-rich ni–coo@peg porous hexagonal nanosheets: Multi-enzyme and ultrasound catalysis for synergistic anticancer treatment, ACS Appl.

Mater. Interfaces. 15 (2023) 13917-13928. https://doi.org/10.1021/acsami.2c20999

[11] C. Huang, X. Lin, T. Lin, W. Lin, Z. Gong, Q. Zheng, B. Li, H. Wang, Multifunctional nanocomposites induce mitochondrial dysfunction and glucose deprivation to boost immunogenic ferroptosis for cancer therapy, Chem.l Eng. J. 466 (2023) 143012. https://doi.org/10.1016/j.cej.2023.143012

[12] Y. Xiong, Z. Yong, C. Xu, Q. Deng, Q. Wang, S. Li, C. Wang, Z. Zhang, X. Yang, Z. Li, Hyperbaric oxygen activates enzyme-driven cascade reactions for cooperative cancer therapy and cancer stem cells elimination, Adv. Sci. 10 (2023) 2301278. https://doi.org/10.1002/advs.202301278

[13] X. Wang, C. Ding, Z. Zhang, C. Li, D. Cao, L. Zhao, G. Deng, Y. Luo, C. Yuan, J. Lu, X. Liu, Degradable nanocatalyst enables antitumor/antibacterial therapy and promotion of wound healing for diabetes via self-enhanced cascading reaction, Chinese Chemical Letters. 34 (2023) 107951. https://doi.org/10.1016/j.cclet.2022.107951

[14] M. Zhang, L. Dong, D. Li, L. Zhu, R. Peng, X. Liu, K. Wang, X. Wang, Y. Zhu, H. Sun, Y. Luo, Sonocatalytic in situ induced oxygen storm precision enhanced reactive oxygen therapy for pancreatic cancer, Adv. Funct. Mater. 33 (2023) 2303451. https://doi.org/10.1002/adfm.202303451

[15] X. Gao, J. Feng, K. Lv, Y. Zhou, R. Zhang, S. Song, H. Zhang, D. Wang, Engineering ceo_2/cuo heterostructure anchored on upconversion nanoparticles with boosting ros generation-primed apoptosis-ferroptosis for cancer dynamic therapy, Nano Res. 16 (2023) 5322-5334. https://doi.org/10.1007/s12274-022-5223-4

[16] M. Zhan, F. Wang, Y. Liu, J. Zhou, W. Zhao, L. Lu, J. Li, X. He, Dual-cascade activatable nanopotentiators reshaping adenosine metabolism for sono-chemodynamic-immunotherapy of deep tumors, Adv. Sci. 10 (2023) 2207200. https://doi.org/10.1002/advs.202207200

[17] Y. Dai, F. Zhang, K. Chen, Z. Sun, Z. Wang, Y. Xue, M. Li, Q. Fan, Q. Shen, Q. Zhao, An activatable phototheranostic nanoplatform for tumor specific nir-ii fluorescence imaging and synergistic nir-ii photothermal-chemodynamic therapy, Small. 19 (2023) 2206053. https://doi.org/10.1002/smll.202206053

[18] Y. Liu, X. Wang, H. Chen, T. Wu, Y. Cao, Z. Liu, Silencing the catalase gene with sirna for enhanced chemodynamic therapy, ACS Appl. Mater. Interfaces. 15 (2023) 8937-8945. https://doi.org/10.1021/acsami.2c20144

[19] Y. Shi, M. Zhou, Y. Zhang, Y. Wang, J. Cheng, Mri-guided dual-responsive anti-tumor nanostructures for synergistic chemo-photothermal therapy and chemodynamic therapy, Acta Biomater. 158 (2023) 571-582. https://doi.org/10.1016/j.actbio.2022.12.053

[20] Z. Liu, S. Liu, B. Liu, Y. Bian, M. Yuan, C. Yang, Q. Meng, C. Chen, P. a. Ma, J. Lin, Fe(iii)-naphthazarin metal–phenolic networks for glutathione-depleting enhanced ferroptosis–apoptosis combined cancer therapy, Small. 19 (2023) 2207825. https://doi.org/10.1002/smll.202207825

[21] X. Feng, T. Lin, D. Chen, Z. Li, Q. Yang, H. Tian, Y. Xiao, M. Lin, M. Liang, W. Guo, P. Zhao, Z. Guo, Mitochondria-associated er stress evokes immunogenic cell death through the ros-perk-eif2α pathway under ptt/cdt combined therapy, Acta Biomater. (2023). https://doi.org/10.1016/j.actbio.2023.02.011

[22] Z. Li, Z. Chu, J. Yang, H. Qian, J. Xu, B. Chen, T. Tian, H. Chen, Y. Xu, F. Wang, Immunogenic cell death augmented by manganese zinc sulfide nanoparticles for metastatic melanoma immunotherapy, ACS Nano. 16 (2022) 15471-15483. https://doi.org/10.1021/acsnano.2c08013

[23] S. Xu, S. Zhou, L. Xie, W. Dou, R. Zhang, B. Zhao, Y. Xu, X. Fu, M. Yuan, A versatile nis2/fes2 hybrid nanocrystal for synergistic cancer therapy by inducing ferroptosis and pyroptosis, Chem.l Eng. J. 460 (2023) 141639. https://doi.org/10.1016/j.cej.2023.141639

[24] D. Cen, Q. Zheng, B. Zheng, R. Zhou, X. Xiao, T. Zhang, Z. Huang, T. Yan, J. Yu, X. Li, R. Deng, X. Cai, A near-infrared light-responsive ros cascade nanoplatform for synergistic therapy potentiating antitumor immune responses, Adv. Funct. Mater. 33 (2023) 2211402. https://doi.org/10.1002/adfm.202211402

[25] C.-Y. Lin, C.-M. Yang, M. Lindén, Influence of serum concentration and surface functionalization on the protein adsorption to mesoporous silica nanoparticles, RSC Adv. 9 (2019) 33912-33921. http://dx.doi.org/10.1039/C9RA05585A

[26] J. Ge, S. Liu, L. Liu, Y. Cui, F. Meng, Y. Li, X. Zhang, F. Wang, Optimizing the electromagnetic wave absorption performance of designed hollow $cofe_2o_4$/cofe@c microspheres, J. Mater. Sci. Technol. 81 (2021) 190-202. https://doi.org/10.1016/j.jmst.2020.10.082

[27] C. Wang, L.-L. Gu, S.-Y. Qiu, J. Gao, Y.-C. Zhang, K.-X. Wang, J.-J. Zou, P.-J. Zuo, X.-D. Zhu, Modulating $cofe_2o_4$ nanocube with oxygen vacancy and carbon wrapper towards enhanced electrocatalytic nitrogen reduction to ammonia, Appl. Catal.B: Environ. 297 (2021) 120452. https://doi.org/10.1016/j.apcatb.2021.120452

[28] S. Hu, X. Sun, Y. Zhao, W. Li, H. Wang, G. Wu, The effective photocatalytic water splitting to simultaneously produce h_2 and h_2o_2 over pt loaded k-g-c_3n_4 catalyst, J. Taiwan Inst. Chem. E. 107 (2020) 129-138. https://doi.org/10.1016/j.jtice.2019.12.007

[29] J. Liu, Z. Sun, Y. D. Dr, Y. Zou, C. Li, X. G. Dr, L. Xiong, Y. Gao, F. L. P. Dr, D. Z. P. Dr., Highly water-dispersible biocompatible magnetite particles with low cytotoxicity

stabilized by citrate groups, Angew. Chem. Int. Ed. 121 (2009) 5989-5993. https://doi.org/10.1002/ange.200901566

[30] Z. Liao, C. Li, Z. Shu, J. Zhou, T. Li, W. Wang, Z. Zhao, L. Xu, L. Shi, L. Feng, K–na co-doping in crystalline polymeric carbon nitride for highly improved photocatalytic hydrogen evolution, Int. J. Hydrog. Energy. 46 (2021) 26318-26328. https://doi.org/10.1016/j.ijhydene.2021.05.138

[31] X. Zhang, P. Ma, C. Wang, L. Gan, X. Chen, P. Zhang, Y. Wang, H. Li, L. Wang, X. Zhou, K. Zheng, Unraveling the dual defect sites in graphite carbon nitride for ultra-high photocatalytic h_2o_2 evolution, Energ. Environ. Sci. 15 (2022) 830-842. http://dx.doi.org/10.1039/D1EE02369A

[32] Z. Cen, Y. Kang, R. Lu, A. Yu, Electrostatic interaction mechanism of visible light absorption broadening in ion-doped graphitic carbon nitride, RSC Adv. 11 (2021) 22652-22660. http://dx.doi.org/10.1039/D1RA02617H

[33] A. Zhang, Y. Guo, H. Xie, Y. Zhang, Y. Fu, C. Ye, Y. Du, M. Zhu, Green and controllable synthesis of kelp-like carbon nitride nanosheets via an ultrasound-mediated self-assembly strategy, J. Colloid Interf. Sci. 628 (2022) 397-408. https://doi.org/10.1016/j.jcis.2022.07.169

[34] C. Dong, X. Dai, X. Wang, Q. Lu, L. Chen, X. Song, L. Ding, H. Huang, W. Feng, Y. Chen, M. Chang, A calcium fluoride nanozyme for ultrasound-amplified and ca^{2+}-overload-enhanced catalytic tumor nanotherapy, Adv. Mater. 34 (2022) 2205680. https://doi.org/10.1002/adma.202205680

[35] L. Zhou, J. Lyu, F. Liu, Y. Su, L. Feng, X. Zhang, Immunogenic panoptosis-initiated cancer sono-immune reediting nanotherapy by iteratively boosting cancer immunity cycle, Adv. Mater. 36 (2024) 2305361. https://doi.org/10.1002/adma.202305361

[36] G. Zhang, M. Zhan, C. Zhang, Z. Wang, H. Sun, Y. Tao, Q. Shi, M. He, H. Wang, J. Rodrigues, M. Shen, X. Shi, Redox-responsive dendrimer nanogels enable ultrasound-enhanced chemoimmunotherapy of pancreatic cancer via endoplasmic reticulum stress amplification and macrophage polarization, Adv. Sci. 10 (2023) 2301759. https://doi.org/10.1002/advs.202301759

[37] L. Shi, Y. Wang, C. Zhang, Y. Zhao, C. Lu, B. Yin, Y. Yang, X. Gong, L. Teng, Y. Liu, X. Zhang, G. Song, An acidity-unlocked magnetic nanoplatform enables self-boosting ros generation through upregulation of lactate for imaging-guided highly specific chemodynamic therapy, Angew. Chem. Int. Ed. 60 (2021) 9562-9572. https://doi.org/10.1002/anie.202014415

[38] J. Yoshida, T. Ohishi, H. Abe, S.-i. Ohba, H. Inoue, I. Usami, M. Amemiya, R. Oriez, C.

Sakashita, S. Dan, M. Sugawara, T. Kawaguchi, J. Ueno, Y. Asano, A. Ikeda, M. Takamatsu, G. Amori, Y. Kondoh, K. Honda, H. Osada, T. Noda, T. Watanabe, T. Shimizu, M. Shibasaki, M. Kawada, Mitochondrial complex i inhibitors suppress tumor growth through concomitant acidification of the intra- and extracellular environment, iScience. 24 (2021) 103497. https://doi.org/10.1016/j.isci.2021.103497

[39] M. Yu, M. Alimujiang, J. U. N. Yin, 611-p: Berberine prevented high-fat diet-induced metabolic disorders via inhibition of whole lipid metabolism, Diabetes. 68 (2019) 611-P. https://doi.org/10.2337/db19-611-P

[40] H. Deng, J. Zhang, Y. Yang, J. Yang, Y. Wei, S. Ma, Q. Shen, Chemodynamic and photothermal combination therapy based on dual-modified metal–organic framework for inducing tumor ferroptosis/pyroptosis, ACS Appl. Mater. Inter. 14 (2022) 24089-24101. https://doi.org/10.1021/acsami.2c00574

[41] F. Yu, T. Wang, Y. Wang, T. Liu, H. Xiong, L. Liu, J. Xiao, X. Liu, H. Jiang, X. Wang, Nanozyme-nanoclusters in metal–organic framework: Gsh triggered fenton reaction for imaging guided synergistic chemodynamic-photothermal therapy, Chem.l Eng. J. (2023) 144910. https://doi.org/10.1016/j.cej.2023.144910

[42] V. Nica, C. Caro, J. M. Páez-Muñoz, M. P. Leal, M. L. Garcia-Martin, Bi-magnetic core-shell $cofe_2o_4$@$mnfe_2o_4$ nanoparticles for in vivo theranostics, Nanomaterials-Basel. 10 (2020). https://doi.org/10.3390/nano10050907

[43] H. Peng, Y.-T. Qin, Y.-S. Feng, X.-W. He, W.-Y. Li, Y.-K. Zhang, Phosphate-degradable nanoparticles based on metal–organic frameworks for chemo-starvation-chemodynamic synergistic antitumor therapy, ACS Appl. Mater. Interfaces. 13 (2021) 37713-37723. https://doi.org/10.1021/acsami.1c10816

[44] Y. Liu, R. Niu, R. Deng, S. Song, Y. Wang, H. Zhang, Multi-enzyme co-expressed dual-atom nanozymes induce cascade immunogenic ferroptosis via activating interferon-γ and targeting arachidonic acid metabolism, J. Am. Chem. Soc. 145 (2023) 8965-8978. https://doi.org/10.1021/jacs.2c13689

[45] S. Zhi, X. Zhang, J. Zhang, X.-y. Wang, S. Bi, Functional nucleic acids-engineered bio-barcode nanoplatforms for targeted synergistic therapy of multidrug-resistant cancer, ACS Nano. 17 (2023) 13533-13544. https://doi.org/10.1021/acsnano.3c02009

[46] Y. Cao, S. Zhang, Z. Lv, N. Yin, H. Zhang, P. Song, T. Zhang, Y. Chen, H. Xu, Y. Wang, X. Liu, G. Zhao, H. Zhang, An intelligent nanoplatform for orthotopic glioblastoma therapy by nonferrous ferroptosis, Adv. Funct. Mater. 32 (2022) 2209227. https://doi.org/10.1002/adfm.202209227

[47] H. Zhu, J. Deng, M. Yuan, X. Rong, X. Xiang, F. Du, X. Luo, C. Cheng, L. Qiu,

Semiconducting titanate supported ruthenium clusterzymes for ultrasound-amplified biocatalytic tumor nanotherapies, Small. 19 (2023) 2206911. https://doi.org/10.1002/smll.202206911

[48] S. Koo, O. K. Park, J. Kim, S. I. Han, T. Y. Yoo, N. Lee, Y. G. Kim, H. Kim, C. Lim, J.-S. Bae, J. Yoo, D. Kim, S. H. Choi, T. Hyeon, Enhanced chemodynamic therapy by cu–fe peroxide nanoparticles: Tumor microenvironment-mediated synergistic fenton reaction, ACS Nano. 16 (2022) 2535-2545. https://doi.org/10.1021/acsnano.1c09171

[49] J. Chen, Z. Zhu, Q. Pan, Y. Bai, M. Yu, Y. Zhou, Targeted therapy of oral squamous cell carcinoma with cancer cell membrane coated co-fc nanoparticles via autophagy inhibition, Adv. Funct. Mater. 33 (2023) 2300235. https://doi.org/10.1002/adfm.202300235

[50] P.-H. Tong, J.-J. Wang, X.-L. Hu, T. D. James, X.-P. He, Metal–organic framework (mof) hybridized gold nanoparticles as a bifunctional nanozyme for glucose sensing, Chem. Sci. 14 (2023) 7762-7769. http://dx.doi.org/10.1039/D3SC02598E

[51] T. Geng, J. Zhang, Z. Wang, Y. Shi, Y. Shi, L. Zeng, Ultrasmall gold decorated bimetallic metal–organic framework based nanoprobes for enhanced chemodynamic therapy with triple amplification, J. Mater. Chem. B. 11 (2023) 2249-2257. http://dx.doi.org/10.1039/D2TB02548E

1